

RESEARCH ARTICLE

TOPOLOGICAL MATTER

Quantum metric nonlinear Hall effect in a topological antiferromagnetic heterostructure

Anyuan Gao¹, Yu-Fei Liu^{1,2}, Jian-Xiang Qiu¹, Barun Ghosh³, Thaïs V. Trevisan^{4,5}, Yugo Onishi⁶, Chaowei Hu⁷, Tiema Qian⁷, Hung-Ju Tien⁸, Shao-Wen Chen², Mengqi Huang⁹, Damien Bérubé¹, Houchen Li¹, Christian Tzschaschel¹, Thao Dinh^{1,2}, Zhe Sun^{1,10}, Sheng-Chin Ho¹, Shang-Wei Lien⁸, Bahadur Singh¹¹, Kenji Watanabe¹², Takashi Taniguchi¹², David C. Bell^{13,14}, Hsin Lin¹⁵, Tay-Rong Chang^{8,16,17}, Chunhui Rita Du⁹, Arun Bansil³, Liang Fu⁶, Ni Ni⁷, Peter P. Orth^{4,5}, Qiong Ma^{10,18}, Su-Yang Xu^{1*}

Quantum geometry in condensed-matter physics has two components: the real part quantum metric and the imaginary part Berry curvature. Whereas the effects of Berry curvature have been observed through phenomena such as the quantum Hall effect in two-dimensional electron gases and the anomalous Hall effect (AHE) in ferromagnets, the quantum metric has rarely been explored. Here, we report a nonlinear Hall effect induced by the quantum metric dipole by interfacing even-layered MnBi₂Te₄ with black phosphorus. The quantum metric nonlinear Hall effect switches direction upon reversing the antiferromagnetic (AFM) spins and exhibits distinct scaling that is independent of the scattering time. Our results open the door to discovering quantum metric responses predicted theoretically and pave the way for applications that bridge nonlinear electronics with AFM spintronics.

Nonlinearities are crucial in many branches of physics, ranging from atomic physics to condensed-matter and complex dynamical systems. Nonlinear electrical transport is the foundation of applications such as rectification and wave mixing. Classically, the most well-known nonlinear device is a PN diode (Fig. 1A). Noncentrosymmetric polar materials (Fig. 1B) are similar to PN diodes as they both possess an electric dipole. They have recently been discovered to show intrinsic nonlinear electrical transport, which may not only lead to new nonlinear applications but also provide a powerful probe of the quantum geometry of the conduction

electrons (1–16). Broadly, the nonlinear transport in both diodes (Fig. 1A) and noncentrosymmetric conductors (Fig. 1B) arises from an inversion asymmetric charge distributions (e.g., an electric dipole). Because the electron has another fundamental degree of freedom, spin, an interesting question is whether spin can also lead to an electrical nonlinearity even in a centrosymmetric lattice. One ideal platform is the class of parity-inversion time-reversal (*PT*)-symmetric antiferromagnets (AFMs) (17), where only the spins feature a noncentrosymmetric distribution (Fig. 1C).

Important clues can be drawn from previous optical experiments, in which optical second-harmonic generation (SHG) has been observed in the *PT*-symmetric AFMs, including Cr₂O₃ and CrI₃ (18). Nevertheless, nonlinear transport is distinct because it directly probes the Fermi surface electrons and in many cases their geometrical properties (1, 2). As such, it enables a probe of the quantum geometry (1, 2) of the topological bands at the Fermi level.

The quantum geometry has two parts, $T = g \cdot i / 2\Omega$ (1) (T is the quantum metric tensor). The imaginary part is the well-known Berry curvature $\Omega_{\alpha\beta} = -2\text{Im} \sum_{m \neq n} [(u_n | i\partial_{k_\alpha} u_m) \langle u_m | i\partial_{k_\beta} u_n \rangle]$,

which describes the curvature of wave function in Hilbert space (n, m are band indices and α, β are spatial directions). Berry curvature has been identified as the source of many unusual electronic and optical responses. By contrast, the real part is the quantum metric, $g_{\alpha\beta} = \text{Re} \sum_{m \neq n} [(u_n | i\partial_{k_\alpha} u_m) \langle u_m | i\partial_{k_\beta} u_n \rangle]$, which measures the distance between neighboring Bloch wave functions in Hilbert space [i.e.,

see section IV.1 of (19)]. Although equally important, the quantum metric is much less explored. There have been a few examples, including the orbital magnetic susceptibilities (20), a third-order Hall effect (13), and the quantum metric in atomic physics (21). However, the way quantum metric regulates electronic motion remains largely unknown. Recently, theories have predicted a wide range of exotic quantum metric responses (20, 22–34).

Here, we report the observation of the quantum metric dipole-induced second-order anomalous Hall effect (AHE) (20, 22–25). In past decades, there have been numerous studies of the AHE (both linear and nonlinear) induced by Berry curvature. Recent theoretical studies, however, predict that the quantum metric can also lead to AHE, thereby advancing our understanding of the fundamental origin of the AHE. Distinct from the Berry curvature-induced AHEs, this effect is predicted to exist in the *PT*-symmetric AFMs (20, 22–25), where *PT* forces the Berry curvature to vanish identically but the effects of quantum metric can manifest strongly. We design and fabricate a feasible material platform and demonstrate the appearance of the quantum metric nonlinear Hall effect (NHE). To conceptualize this type of NHE, we draw comparison with the well-known AHE in ferromagnetic metals (35), where Berry curvature leads to the anomalous velocity and therefore the AHE, $v_{\text{anomalous}} \propto \int_{\mathbf{k}} \mathbf{E}_{\parallel} \times$

$\mathbf{\Omega}(\mathbf{E}_{\parallel})$ is the in-plane source-drain electric field). By contrast, in a *PT*-symmetric AFM, Berry curvature is zero as dictated by *PT*. However, a nonzero quantum metric g can induce an anomalous velocity to second order in \mathbf{E}_{\parallel} , $v_{\text{anomalous}} \propto \int_{\mathbf{k}} \mathbf{E}_{\parallel} \times [\nabla_{\mathbf{k}} \times (g\mathbf{E}_{\parallel})]$, as proposed

in (20). This leads to an intrinsic second-order Hall effect. From the expression above, one can show that this effect is nonzero only when the system breaks both *P* and *T*. Therefore, we need *PT*-symmetric AFM conductors with a large quantum metric on the Fermi surface. We have carefully considered possible materials, and identified two-dimensional (2D) even-layered MnBi₂Te₄ (15, 36–46) as an ideal platform. Even-layered MnBi₂Te₄ is a *PT*-symmetric AFM. Moreover, its topological bands support gate-tunable transport and a giant quantum metric (19). However, its lattice has C_{3v} rotational symmetry (Fig. 1, D and E), which forces the effect to vanish (22). To break C_{3v} , we interface MnBi₂Te₄ with black phosphorus (BP) (47).

Demonstration of rotational symmetry breaking

We start by showing that interfacing MnBi₂Te₄ with BP indeed breaks its C_{3v} rotational symmetry. To this end, we study the directional dependence of the resistance (6) of MnBi₂Te₄ without and with BP. We fabricated a six-septuple-layer

¹Department of Chemistry and Chemical Biology, Harvard University, Cambridge, MA 02138, USA. ²Department of Physics, Harvard University, Cambridge, MA 02138, USA. ³Department of Physics, Northeastern University, Boston, MA 02115, USA. ⁴Department of Physics and Astronomy, Iowa State University, Ames, IA 50011, USA. ⁵Ames National Laboratory, Ames, IA 50011, USA. ⁶Department of Physics, Massachusetts Institute of Technology, Cambridge, MA 02139, USA. ⁷Department of Physics and Astronomy and California NanoSystems Institute, University of California, Los Angeles, Los Angeles, CA 90095, USA. ⁸Department of Physics, National Cheng Kung University, Tainan 701, Taiwan. ⁹Department of Physics, University of California San Diego, La Jolla, CA, 92093, USA. ¹⁰Department of Physics, Boston College, Chestnut Hill, MA, USA. ¹¹Department of Condensed Matter Physics and Materials Science, Tata Institute of Fundamental Research, Colaba, Mumbai, India. ¹²International Center for Materials Nanoarchitectonics, National Institute for Materials Science, 1-1 Namiki, Tsukuba 305-0044, Japan. ¹³Harvard John A. Paulson School of Engineering and Applied Sciences, Harvard University, Cambridge, MA 02138, USA. ¹⁴Center for Nanoscale Systems, Harvard University, Cambridge, MA 02138, USA. ¹⁵Institute of Physics, Academia Sinica, Taipei 11529, Taiwan. ¹⁶Center for Quantum Frontiers of Research and Technology (QFort), Tainan 701, Taiwan. ¹⁷Physics Division National Center for Theoretical Sciences, Taipei 10617, Taiwan. ¹⁸Canadian Institute for Advanced Research, Toronto, Canada. *Corresponding author. Email: suyangxu@fas.harvard.edu

(6SL) MnBi_2Te_4 device with radially distributed electrical contacts (Device-BM1). The four-probe resistance ($T = 1.8$ K) is found to be isotropic (Fig. 1G, blue curve), consistent with the C_{3z} symmetry. We then stacked a BP layer (~ 10 nm) onto this MnBi_2Te_4 sample and performed the measurements again. The resistance develops a clear anisotropy with a 180° periodicity (Fig. 1G, red curve), providing a clear signature of the breaking of C_{3z} [section I.4 of (19) shows that the transport is dominated by the MnBi_2Te_4 layer of the heterostructure]. The transverse resistance and two-probe resistance also show the breaking of C_{3z} [fig. S12 of (19)]. We further substantiate the breaking of C_{3z} symmetry by an independent method, the optical SHG, at room temperature. As shown in Fig. 1H, our SHG data also show the clear breaking of C_{3z} symmetry [see detailed discussions in section I.5 of (19)]. Our demonstration of C_{3z} breaking establishes the BP/ MnBi_2Te_4 heterostructure as an ideal platform to search for this effect.

Observation of the nonlinear Hall effect

To measure the linear and nonlinear electrical transport, we pass a current at frequency ω (I^ω) and use the lock-in technique to detect linear voltage V^ω and nonlinear voltage $V^{2\omega}$. We describe the nonlinear voltage as $V_{ijk}^{2\omega}$, where i is the direction of the nonlinear voltage $V^{2\omega}$ and j, k are the directions of the injected current I^ω . All measurements are performed at $B = 0$.

Figure 1I shows the nonlinear Hall voltage $V_{yxx}^{2\omega}$ of the Device-BM1 before and after being interfaced with BP. A prominent nonlinear Hall signal emerges only after BP is introduced. This is in sharp contrast to the linear voltage (Fig. 1I, inset), which becomes even slightly smaller upon the introduction of BP. Such observation agrees well with the theoretical expectation of the intrinsic NHE induced by a quantum metric dipole. To exclude that the effect is caused by a Berry curvature dipole (4, 6, 7, 9), we study the relationship between the second-order NHE and the AFM order in MnBi_2Te_4 .

The AFM spin-induced nonlinearity

Overall, we have fabricated 30 BP/even-layered MnBi_2Te_4 heterostructure devices [see section I.0 of (19) for our systematic data that confirm the MnBi_2Te_4 thickness in our devices]. In all of the 30 devices, we have observed the NHE with consistent behaviors as a function of AFM order, spatial direction, scattering time, vertical electric field, and doping [see fig. S22 and table S1 for a summary of all 30 devices (19)]. Here, we focus on the Device-BMB1 (Fig. 2A), which has two-layer BP on both sides of six-septuple-layer MnBi_2Te_4 . Moreover, we have ensured that the crystalline a axes of the BPs and the MnBi_2Te_4 are aligned (Fig. 2A). Such a carefully controlled configuration is important to preserve MnBi_2Te_4 's PT symmetry, which en-

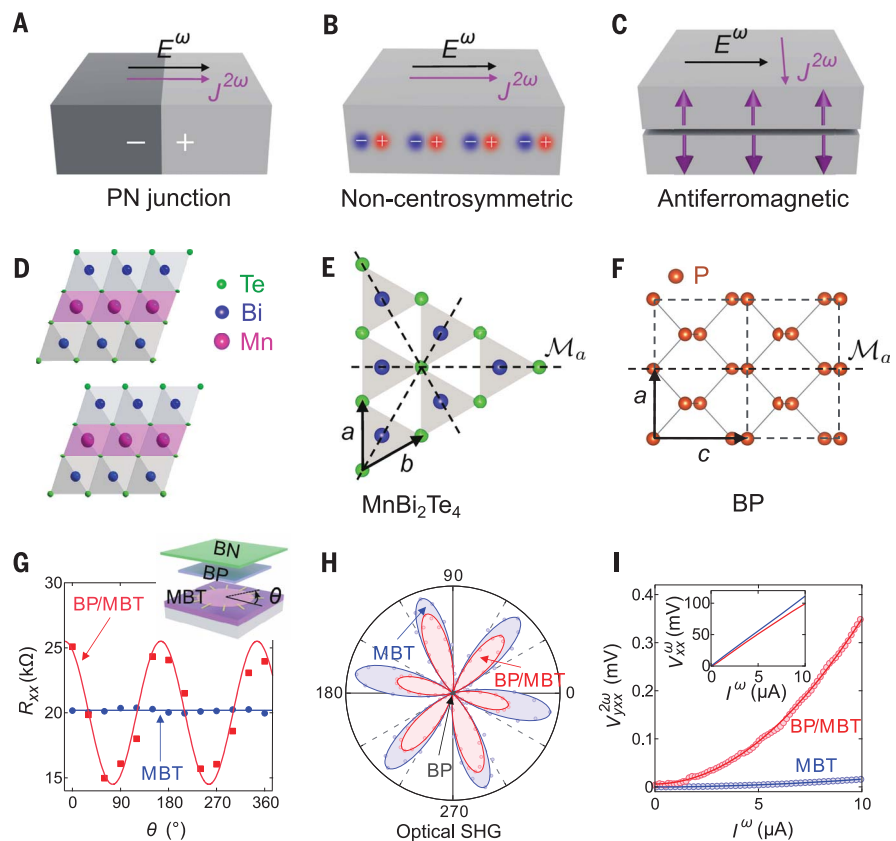


Fig. 1. Spin-induced electrical nonlinearity in PT -symmetric antiferromagnets and introduction to our sample. (A and B) Nonlinear electrical transport in PN junctions and noncentrosymmetric conductors (charge-induced electrical nonlinearity). (C) Nonlinear electrical transport in PT -symmetric AFMs (spin-induced electrical nonlinearity). (D to F) Lattice structures of the MnBi_2Te_4 and BP. (G and H) Angle-resolved resistance and optical SHG measurements of a 6SL MnBi_2Te_4 before and after being interfaced with BP. (I) The nonlinear Hall signal $V_{xx}^{2\omega}$ before and after being interfaced with BP at $B = 0$ T. Inset: The linear longitudinal voltage V_{xx}^ω before and after being interfaced with BP. All data in Figs. 1 to 4 were taken at temperature $T = 1.8$ K unless otherwise noted. Data in Fig. 1 and Fig. 2B are from Device-BM1. Data in Fig. 2, E to J, Fig. 3, and Fig. 4A are from Device-BMB1. Data in Fig. 4F are from Device-BM21.

sures that the Berry curvature and Berry curvature dipole vanish. Figure 2B shows a large transverse nonlinear response $V_{yxx}^{2\omega}$. We have also measured the longitudinal nonlinear response $V_{xxx}^{2\omega}$, which shows no observable signal. Therefore, our data reveal an interesting “Hall dominance” in the nonlinear transport.

We now focus on exploring how the nonlinear Hall signal depends on opposite AFM states. In ferromagnets, the opposite ferromagnetic states can be controlled by sweeping the B field. In PT -symmetric AFMs including Cr_2O_3 , even-layered CrI_3 , and even-layered MnBi_2Te_4 (44, 48, 49), previous works have shown that the opposite AFM states can be controlled by sweeping the vertical B_z field under a fixed vertical E_z field. Hence, we follow the previously established procedures (44): Under a fixed E_z ($E_z = -0.17$ V/nm), we sweep B_z from -8 T to 0 T or from $+8$ T to 0 T to prepare the two AFM states (Fig. 2, C and D). We first study the AFM I. The linear voltage V_{xx}^ω (Fig. 2E) exhibits a typical ohmic behavior. The

nonlinear voltage $V_{yxx}^{2\omega}$ (Fig. 2G) is prominent and its sign is positive. We then prepare AFM II. The linear voltage V_{xx}^ω (Fig. 2F) remains unchanged. In sharp contrast, the nonlinear voltage $V_{yxx}^{2\omega}$ (Fig. 2H) flips sign. For both AFM I and II, the NHE is only present in the AFM phase (Fig. 2, I and J). Our observation that the nonlinear Hall signal flips sign upon reversing the AFM order further demonstrates its quantum metric dipole origin, because the quantum metric dipole is theoretically expected to be opposite for the opposite AFM domains [see section III of (19)]. Our nonlinear Hall signal measures an average over all AFM domains. However, our experiments suggest that our sample is prepared into predominantly one domain. If our sample consisted of opposite domains with a 50%-50% composition, then the measured nonlinear Hall signal would average to zero. By contrast, our data show a large nonzero nonlinear Hall signal. Moreover, the sign of the observed signal flips as we prepare the opposite AFM domain.

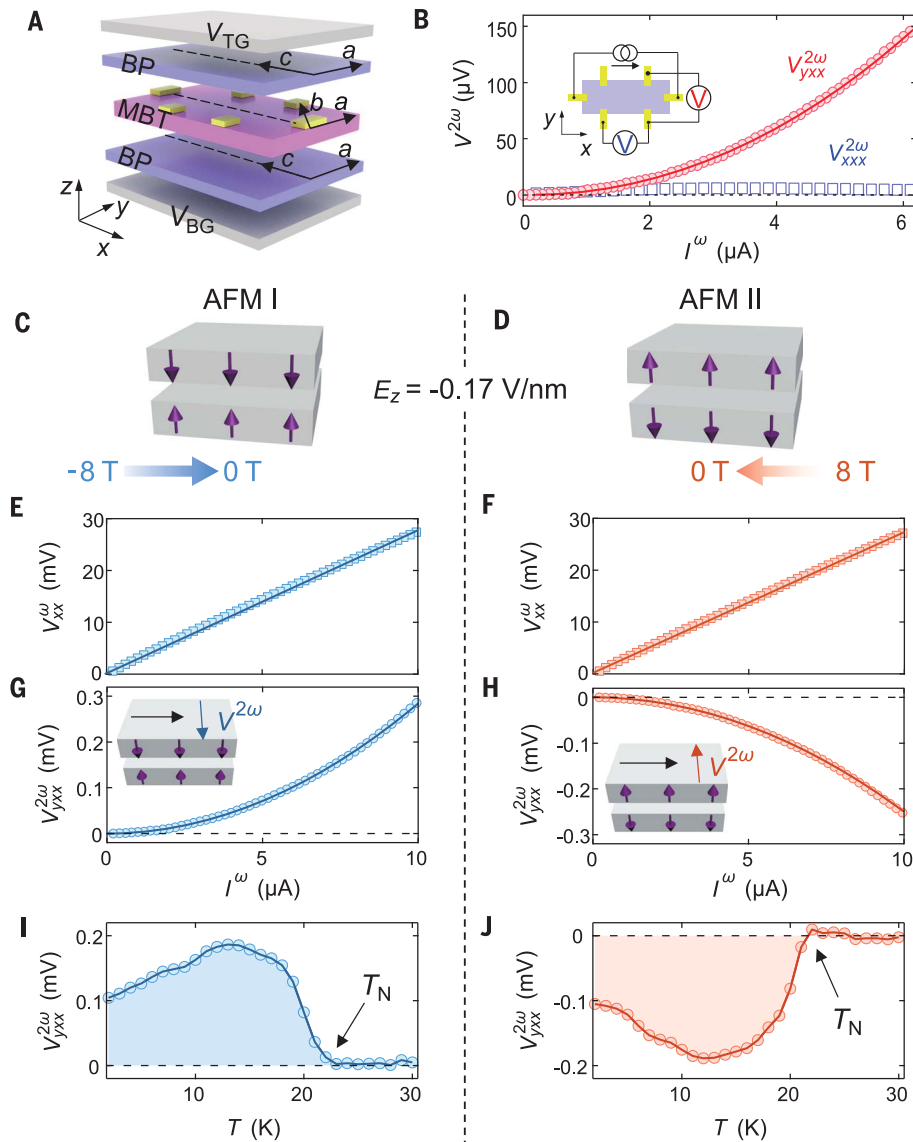


Fig. 2. Observation of the antiferromagnetic NHE. (A) Schematic illustration of 2L BP/6SL MnBi₂Te₄/2L BP device (Device-BMB1). The crystalline *a* axes of the BPs and the MnBi₂Te₄ were all aligned [fig. S16 of (19)]. (B) The longitudinal ($V_{xx}^{2\omega}$) and Hall ($V_{yxx}^{2\omega}$) components of the nonlinear voltage. (C and D) We follow the procedures established by previous works (44): Under a fixed E_z (−0.17 V/nm), we sweep B_z from −8 T to 0 T or from +8 T to 0 T to prepare the two AFM states. (E and F) Linear longitudinal voltage as a function of incidence current for AFM I and AFM II. (G and H) Nonlinear Hall voltage as a function of incident current and temperature of AFM I, respectively. (I and J) The same as panels (G) and (I) but for AFM II.

Further, the magnitude of the measured signal is consistent with the theoretically calculated value, which assumes a single domain. Spatially resolved magnetic measurements will be needed to determine the exact domain composition.

We now perform further systematic studies. Because the nonlinear Hall current flips sign upon reversing the AFM order, all the nonlinear Hall data (apart from Fig. 2) are obtained by taking the difference between the two AFM domains. First, the intrinsic NHE is expected to be independent of the scattering time, unlike other related responses. Similar to the intrinsic AHE in ferromagnetic metals

(35), and in contrast to the quantum AHE, there is still dissipation through the linear Drude conductivity σ_{xx} . The nonlinear Hall conductivity can be directly extracted from our data by $\sigma_{yxx}^{2\omega} = J_{yxx}^{2\omega}/E_x^{\omega 2} = (V_{yxx}^{2\omega} l^3)/(I_x^{\omega 2} R_{xx}^3 \omega^2 d)$, where l , w , d are the length, width, and thickness of the sample. Previous experiments have studied the scattering time τ dependence of various Hall effects (6, 9, 14, 35) by investigating the scaling between the corresponding Hall conductivity and the Drude conductivity. Following this established method, we study the scaling between $\sigma_{yxx}^{2\omega}$ and σ_{xx} . Our data (Fig. 3A) show that $\sigma_{yxx}^{2\omega}$ is independent of σ_{xx} below

~15 K. Moreover, consistent results have been observed at multiple charge densities in the same sample and from different samples [section III.9 of (19)]. These systematic data point to the conclusion that the $\sigma_{yxx}^{2\omega}$ is independent of scattering time τ below ~15 K. Above ~15 K, $\sigma_{yxx}^{2\omega}$ vanishes quickly across Néel temperature T_N because the AFM order vanishes and our NHE only exists in the AFM phase. Hence, studying the τ dependence at temperatures near T_N would require one to take the strong influence of the AFM order near T_N into account [see section III.8 of (19) for additional measurements and analysis]. Second, the intrinsic NHE does not require a noncentrosymmetric lattice or any explicit breaking of *PT* symmetry. To test this, we explicitly break *PT* by applying a vertical E_z field via dual gating. The nonlinear Hall signal is already prominent even at $E_z = 0$ (Fig. 3D), confirming that it does not require any *PT* breaking. Moreover, the nonlinear Hall signal is symmetric for $\pm E_z$, also consistent with the expectation [see section IV.2 of (19)]. Third, the NHE is expected to be sensitive to the direction of the incident current I^ω . In Fig. 3B, we measure the nonlinear Hall conductivity as a function of the direction of I^ω . Indeed, the signal is most prominent when I^ω is along a particular in-plane direction. In this way, we experimentally mapped out the direction of the relevant geometrical dipole (the quantum metric dipole in our case, as we demonstrate next). Moreover, the intrinsic NHE is found to be independent of frequency [fig. S23 of (19)]. In principle, the frequency independence is expected to persist until ω is large enough to induce an interband transition (roughly terahertz or far-infrared). Future experiments are needed to test the NHE in that regime.

Excluding competing mechanisms

Although we tried to eliminate Berry curvature dipole by aligning the crystalline *a* axes between BPs and MnBi₂Te₄ to preserve *PT* symmetry (Fig. 2A), let us assume that the alignment is imperfect, so Berry curvature dipole is allowed. We now show that the observed relationship between the nonlinear Hall signal and AFM order can distinguish between Berry curvature dipole D_{Berry} and quantum metric dipole D_{Metric} . D_{Berry} can be understood as a distribution of the Berry curvature around the Fermi surface such that it is larger on one side of the Fermi surface than on the opposite side. A similar picture holds for D_{Metric} (Fig. 3). As we observe that the nonlinear Hall signal changes sign upon the reversal of AFM order, the dipole that causes our observed nonlinear Hall signal must also flip. Let us assume that the AFM I has $D_{\text{Berry}} > 0$ and $D_{\text{Metric}} > 0$, which is visualized in a tilted gapped Dirac band structure in Fig. 3, E and G. We now flip the AFM order to the AFM II by performing

time reversal T . Under T , the bands are flipped between $\pm\mathbf{k}$ (Fig. 3, F and H), the Berry curvature flips sign, but the quantum metric keeps the same sign. Hence, from Fig. 3, F and H, one can see that, $D_{\text{Berry}}(\text{AFMII}) = D_{\text{Berry}}(\text{AFMI})$, but $D_{\text{Metric}}(\text{AFMII}) = -D_{\text{Metric}}(\text{AFMI})$. Therefore, our observation that the nonlinear Hall signal flips sign upon reversing the AFM order excludes the Berry curvature dipole mechanism. In section II.1 of (19), we enumerate experimental results, including the relation with AFM order, scaling, vertical electric field dependence, and relation with mirror symmetry, which corroborate that the Berry curvature dipole mechanism cannot account for our data.

Within the nonlinear effects that flip sign upon reversing the AFM order, there is another possibility, the second-order Drude effect (5, 12, 17, 22). This effect is expected to be proportional to τ^2 (22) and therefore can be ruled out on the basis of our scaling data in Fig. 3A. Moreover, the NHE is antisymmetric (upon exchanging the first two indices), $\sigma_{\alpha\beta\gamma}^{\text{NHE}} = -\sigma_{\beta\alpha\gamma}^{\text{NHE}}$, but the second-order Drude effect (SODE) is symmetric, $\sigma_{\alpha\beta\gamma}^{\text{SODE}} = \sigma_{\beta\alpha\gamma}^{\text{SODE}}$ (22). Using an electrical sum-frequency generation method [section II.2 of (19)], we showed that our signal is indeed antisymmetric, $\sigma_{yx}^{2\omega} = -\sigma_{xy}^{2\omega}$, which demonstrates that the SODE is insignificant in our signal. In section II.2.3 of (19), we present additional data that suggest that the NHE is dominant over the SODE at different temperatures and charge densities. In section III.5 of (19), we show that the nonlinear Hall signal is negligibly small at ± 8 T because the forced ferromagnetic state recovers inversion symmetry. We also carefully addressed other competing origins such as thermal and accidental diode junctions [section II.3 of (19)].

Energy-resolved probe of quantum metric in PT -symmetric antiferromagnets

We also study the evolution of the nonlinear conductivity $\sigma_{yx}^{2\omega}$ with the charge density. The nonlinear Hall signal is zero inside the charge neutrality gap (Fig. 4A). This is consistent with the expectation that the NHE is a Fermi surface property. As we tune the Fermi energy away from the charge neutrality, the nonlinear Hall signal emerges. Notably, the conductivities in electron and hole regimes have the same sign. As we go deeper into the electron-doped regime, the signal reverses sign.

We now provide an intuitive physical picture to understand the large quantum metric dipole and its Fermi-level dependence. MnBi_2Te_4 features Dirac surface states, which are gapped owing to the AFM, leading to a large quantum metric near the gap edge. Moreover, because the AFM order breaks both T and P , the Dirac bands are asymmetric about $\mathbf{k} = 0$ (Fig. 3G). Hence, at a fixed energy, positive and negative momenta have a different quantum metric, leading to a nonzero quantum metric dipole.

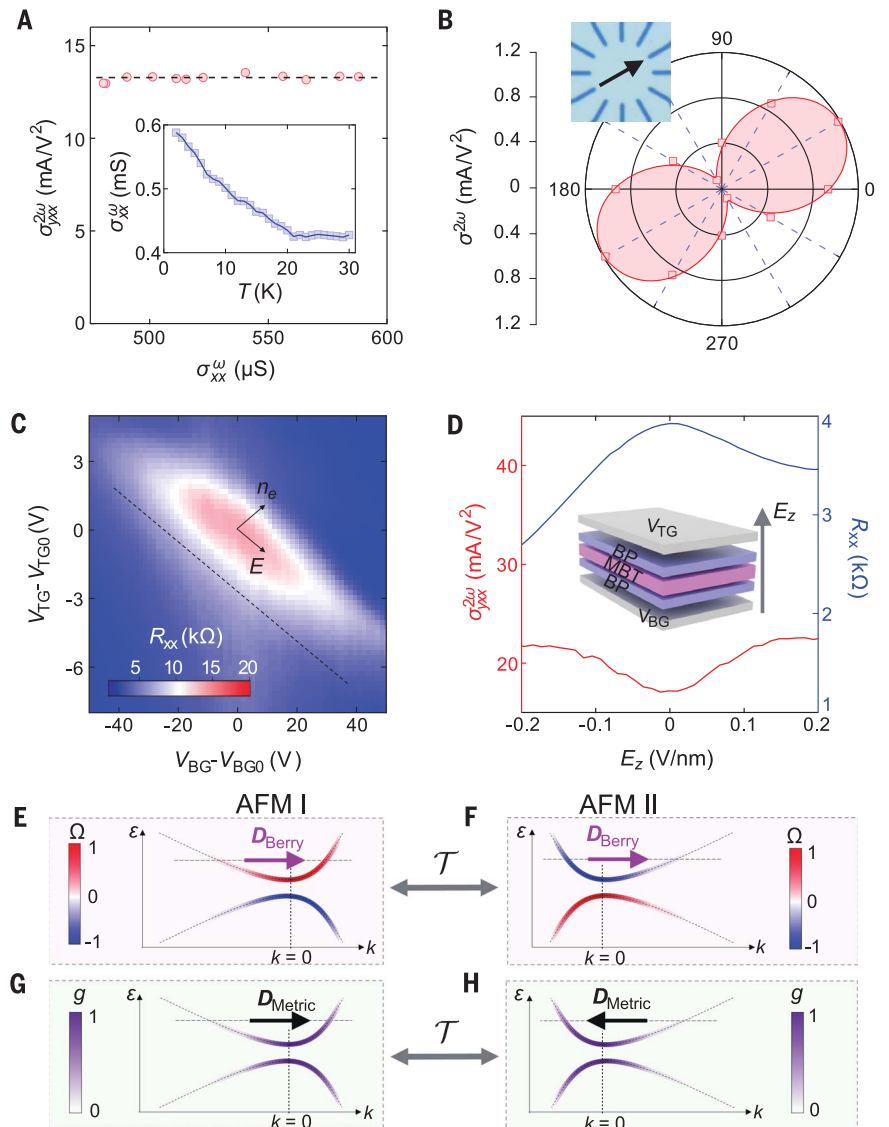


Fig. 3. Systematic investigation of the NHE. (A) The scaling between the nonlinear Hall conductivity and the Drude conductivity $\sigma_{xx} = 1/R_{xx}$. The nonlinear Hall conductivity can be directly extracted from the data as $\sigma_{yx}^{2\omega} = j_{yx}^{2\omega}/E_x^2 = (V_{yx}^{2\omega}\beta^3)/(I_x^2 R_{xx}^3 w^2 d)$. (B) Angular dependence of the nonlinear Hall conductivity in Device-BM1. (C) Dual-gated resistance map of the 2L BP/6SL MnBi_2Te_4 /2L BP heterostructure (Device-BMB1). The vertical electric field E_z and charge density dependence can be independently tuned by combining the top and bottom gate voltages. (D) E_z dependence of the nonlinear Hall conductivity and linear longitudinal resistance. E_z follows the dashed line in (C). (E to H) Schematic illustration of the Berry curvature dipole (D_{Berry}) and the quantum metric dipole (D_{Metric}) for the AFM I and AFM II of the BP/6SL MnBi_2Te_4 /BP heterostructure (see text). Although we aligned the crystalline axes of BP and MnBi_2Te_4 in our Device-BMB1 (Fig. 2A), realistically it is difficult to make the alignment perfect. If the alignment is imperfect and PT symmetry is broken, a Berry curvature dipole is allowed.

Intuitively, we can understand the sign of the nonlinear Hall signal by considering whether positive or negative momenta have a larger quantum metric. We see from Fig. 3G that both upper and lower parts of the Dirac cone have $g(+k_F) > g(-k_F)$, suggesting that the nonlinear Hall signals should show the same sign in electron and hole regimes, consistent with our data (Fig. 4A). The sign change in the electron-doped regime is beyond this simple picture.

To achieve a more comprehensive understanding, we built an effective model of the BP/6SL MnBi_2Te_4 /BP heterostructure [section IV.4-9 of (19)]. Owing to the incommensurability of the BP and MnBi_2Te_4 lattices, we need to derive the coupling between the Bloch states of the two materials in the real-space continuum [i.e., within the extended Brillouin zone (BZ)]. The low-energy bands are located in the BZ center, so only Bloch

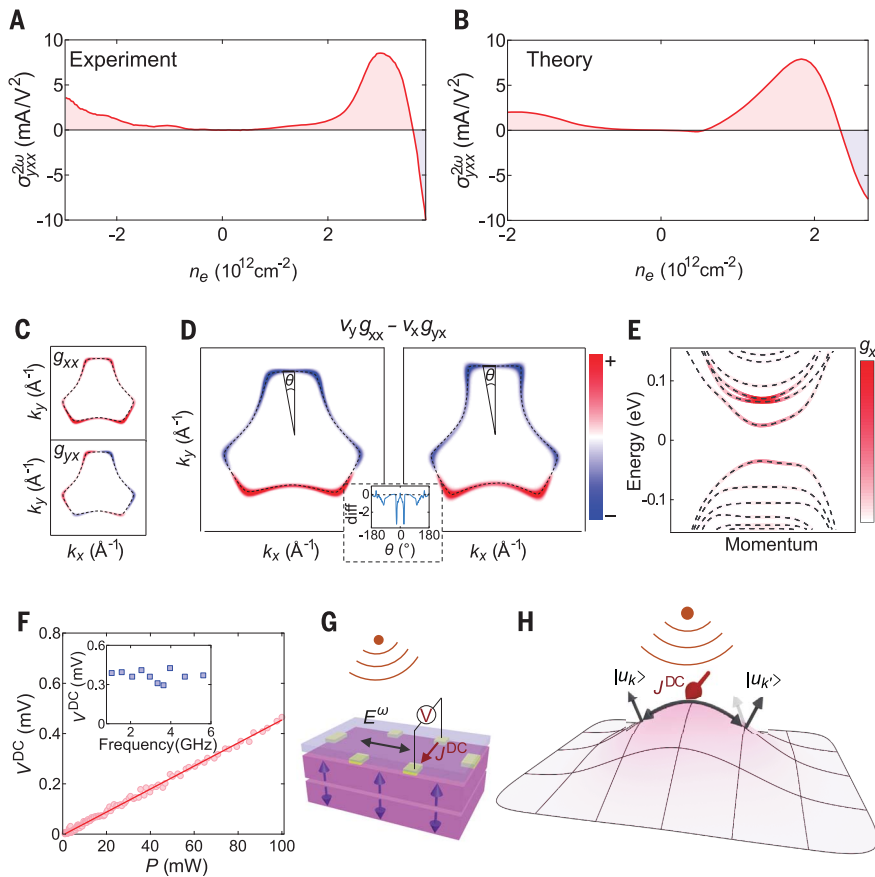


Fig. 4. The quantum metric dipole as the microscopic geometrical origin. (A) Experimentally measured nonlinear Hall conductivity as a function of charge density. (B) Theoretically calculated $\sigma_{yxx}^{2\omega}$ as a function of n_e based on the BP/6SL MnBi₂Te₄/BP band structure (see text). (C to E) The electronic structure of the BP/6SL MnBi₂Te₄/BP heterostructure calculated with an effective model (see text). (C) Fermi surface at -50 meV (the lower part of the surface Dirac cone). The coupling between MnBi₂Te₄ and BP is turned off, so that contour respects C_{3z} symmetry. The quantum metric g_{xx} and g_{yx} plotted around the Fermi surface. (D) The nonlinear Hall conductivity is given by the integral $D_{\text{Metric}} = \int_{\mathbf{k}} (v_y g_{xx} - v_x g_{yx}) \delta(\epsilon - \epsilon_F)$ around the Fermi surface. With C_{3z} symmetry (left panel), the integral goes to zero. After turning on the coupling between MnBi₂Te₄ and BP (right panel), C_{3z} is broken, making the integral around the Fermi contour nonzero. To more clearly see how the integral changes to nonzero when C_{3z} is broken, we rewrite D_{Metric} as an integral of the polar angle θ , $D_{\text{Metric}} = \int_{\text{FS}} (v_y g_{xx} - v_x g_{yx}) \frac{dl}{d\theta} d\theta$ (dl is an infinitesimal length along the Fermi surface).

The inset presents the change of the above kernel [see section III.16 of (19) for details]. (E) Band structure of BP/6SL MnBi₂Te₄/BP heterostructure as a function of k_y for $k_x = 0$. Color represents the quantum metric of the bands. (F) Measured microwave rectification based on the intrinsic NHE. Inset: DC signal as a function of microwave frequency. (G) Schematic illustration of microwave rectification. (H) Schematic illustration of quantum metric-induced nonlinear responses. The horizontal axes are k_x and k_y . The two black arrows represent the Bloch wave functions at two nearby k points. The two arrows point to different directions, illustrating a finite distance between two wave functions (i.e., a finite quantum metric). This quantum metric leads to a NHE, which can turn an external AC electric field (e.g., the microwave in the figure) into a DC signal.

bands with the same momentum hybridize. The coupling amplitude depends only on the characteristic decay length of the atomic orbitals as any discrete lattice structure is averaged out (47). The Hamiltonian reads

$$\hat{h}(k_x, k_y) = \begin{pmatrix} \hat{h}_{\text{MBT}} & \hat{U}_t & \hat{U}_b \\ \hat{U}_t^\dagger & \hat{h}_{\text{BP}, t} & 0 \\ \hat{U}_b^\dagger & 0 & \hat{h}_{\text{BP}, b} \end{pmatrix}. \hat{h}_{\text{MBT}} \text{ and } \hat{h}_{\text{BP}, t(b)}$$

by fitting the first-principle band structures. The MnBi₂Te₄ and BP coupling parameters were partly constrained by considering the independent data of R_{xx}/R_{yy} so that an agreement in the overall magnitude was achieved independently. We adjusted the remaining free coupling model parameters to match detailed features in the charge density dependence [section IV.9 of (19)].

We first turn off the coupling between the MnBi₂Te₄ and BP. The Fermi surface shown in Fig. 4C (-50 meV) is C_{3z} symmetric, and there is already a large quantum metric (g_{xx} and g_{yx}) around it. According to (22), the D_{Metric} responsible for the nonlinear Hall is given by $D_{\text{Metric}} = \int_{\mathbf{k}} (v_y g_{xx} - v_x g_{yx}) \delta(\epsilon - \epsilon_F)$ (v is the Fermi velocity). We plot the integral kernel in color in Fig. 4D. Positive and negative contributions around the contour exactly cancel each other out because of C_{3z} symmetry. So, the integral goes to zero (Fig. 4D, left panel). We then turn on the MnBi₂Te₄-BP couplings, which breaks C_{3z} . For the C_{3z} -breaking contour, we observe unequal contributions from the two colors, leading to a nonzero D_{Metric} [Fig. 4D, right panel; see details in the caption and in section III.16 of (19)]. Figure 4E shows the band structure of the BP/6SL MnBi₂Te₄/BP heterostructure, from which we can compute the intrinsic nonlinear Hall conductivity $\sigma_{yxx}^{2\omega}$ as a function of chemical potential. In particular, near the charge neutrality gap, we found that $\sigma_{yxx}^{2\omega}$ indeed mainly comes from the quantum metric of the Dirac surface states, consistent with the intuitive picture above. The sign inversion in the electron-doped regime mainly comes from the quantum metric of the avoided crossing inside conduction bands according to our calculation [section IV.9 of (19)]. Owing to the multiband nature of our model, the $\sigma_{yxx}^{2\omega}$ was calculated by the general expression

$$\sigma_{yxx}^{2\omega} = -2e^3 \sum_{n,m}^{\epsilon_m \neq \epsilon_n} \text{Re} \int_{\mathbf{k}} \left(\frac{v_y^n \langle u_n | i\partial_{k_x} u_m \rangle \langle u_m | i\partial_{k_x} u_n \rangle}{\epsilon_n - \epsilon_m} - \frac{v_x^n \langle u_n | i\partial_{k_y} u_m \rangle \langle u_m | i\partial_{k_y} u_n \rangle}{\epsilon_n - \epsilon_m} \right) \delta(\epsilon_n - \epsilon_F) \quad (22).$$

This general expression can be decomposed into the quantum metric dipole contribution plus additional interband contributions (AIC)

$$\sigma_{yxx}^{2\omega} = -2e^3 \sum_n \int_{\mathbf{k}} \left(\frac{v_y^n g_{xx}^n}{\epsilon_n - \epsilon_n} - \frac{v_x^n g_{yx}^n}{\epsilon_n - \epsilon_n} \right) \delta(\epsilon_n - \epsilon_F) + \text{AIC} \quad (1)$$

where the first term is the quantum metric dipole contribution, and the second term is

$$\text{AIC} = -2e^3 \sum_{n,m}^{\epsilon_m \neq \epsilon_n, \epsilon_n} \text{Re} \int_{\mathbf{k}} \left(\frac{v_y^n \langle u_n | i\partial_{k_x} u_m \rangle \langle u_m | i\partial_{k_x} u_n \rangle}{\epsilon_n - \epsilon_m} - \frac{v_x^n \langle u_n | i\partial_{k_y} u_m \rangle \langle u_m | i\partial_{k_y} u_n \rangle}{\epsilon_n - \epsilon_m} \right) \delta(\epsilon_n - \epsilon_F) \quad (\bar{n} \text{ is the band whose energy is closest to } n).$$

In our BP/6SL MnBi₂Te₄/BP system, we found that the quantum metric dipole contribution strongly dominates, whereas the AIC is small [details

in section IV.3 of (19)]. Therefore, our non-linear Hall measurement is a powerful, energy-resolved probe of the quantum metric.

Possible AFM spin-based wireless rectification

The second-order nonlinear effect enables not only frequency doubling but also rectification. We use the intrinsic AFM nonlinear Hall effect to demonstrate wireless rectification with zero external bias (battery-free) and without magnetic field. We inject microwave radiation and measure the DC signal. We observe clear rectification DC voltage in response to the microwave radiation (Fig. 4F), which shows a broad band response, including the Wi-Fi frequencies (2.4 and 5 GHz) and even higher frequencies [see fig. S35 and section V.2 of (19)]. In section III.12 of (19), we show that the rectification signal flips sign as we reverse the AFM state, which suggests the intrinsic quantum metric dipole origin. Apart from the intrinsic quantum metric dipole, extrinsic sources such as the Schottky diodes at the metal-MnBi₂Te₄ junction, unintentional diodes inside the MnBi₂Te₄, and the gap between the two gates can also lead to microwave rectification. To unambiguously rule out these extrinsic sources, future systematic experiments will be needed [discussion in section V.1 of (19)].

Discussion and outlook

The intrinsic second-order Hall effect observed here realizes an electrical nonlinearity induced by the AFM spins and provides a rare example of a quantum metric response. As highlighted by recent theoretical studies, the influence of the quantum metric is expected to span many different areas, ranging from nonlinear responses in *PT*-symmetric AFMs to flat-band conductivity, superconductivity and charge orders in moiré systems, the fractional Chern insulator, and *k*-space dual of gravity (20, 22–34). Another interesting future direction is to explore the nonlinear responses in canted AFM materials [section V.3 of (19)], where nonzero Berry curvature of higher order in magnetization has recently been observed (38, 46, 51). In terms of materials, we show that, beyond “band structure engineering,” the van der Waals interfaces can engineer the properties of the wave function i.e., “quantum geometry engineering” (47). Our observations may enable the use of AFM spins to harvest electromagnetic energy and to realize self-powered AFM spintronic devices. An exciting future breakthrough would be to demonstrate room-temperature wireless rectification based on the quantum metric NHE in a *PT*-symmetric AFM material.

REFERENCES AND NOTES

1. J. Provost, G. Vallee, *Commun. Math. Phys.* **76**, 289–301 (1980).
2. Y. Tokura, N. Nagaosa, *Nat. Commun.* **9**, 3740 (2018).

3. J. E. Moore, J. Orenstein, *Phys. Rev. Lett.* **105**, 026805 (2010).
4. I. Sodemann, L. Fu, *Phys. Rev. Lett.* **115**, 216806 (2015).
5. T. Ideue et al., *Nat. Phys.* **13**, 578–583 (2017).
6. K. Kang, T. Li, E. Sohn, J. Shan, K. F. Mak, *Nat. Mater.* **18**, 324–328 (2019).
7. Q. Ma et al., *Nature* **565**, 337–342 (2019).
8. S. Dzsaber et al., *Proc. Natl. Acad. Sci. U.S.A.* **118**, e2013386118 (2021).
9. D. Kumar et al., *Nat. Nanotechnol.* **16**, 421–425 (2021).
10. K. Yasuda et al., *Nat. Nanotechnol.* **15**, 831–835 (2020).
11. W. Zhao et al., *Nat. Mater.* **19**, 503–507 (2020).
12. H. Isobe, S.-Y. Xu, L. Fu, *Sci. Adv.* **6**, eaay2497 (2020).
13. S. Lai et al., *Nat. Nanotechnol.* **16**, 869–873 (2021).
14. P. He et al., *Nat. Nanotechnol.* **17**, 378–383 (2022).
15. Z. Zhang et al., *Nat. Commun.* **13**, 6191 (2022).
16. S. Sinha et al., *Nat. Phys.* **18**, 765–770 (2022).
17. N. J. Zhang et al., Momentum polarized superconductivity in twisted trilayer graphene. Preprint at <https://arxiv.org/abs/2209.12964> (2022).
18. Z. Sun et al., *Nature* **572**, 497–501 (2019).
19. See additional text and data in the supplementary materials.
20. Y. Gao, S. A. Yang, Q. Niu, *Phys. Rev. Lett.* **112**, 166601 (2014).
21. A. Gianfrate et al., *Nature* **578**, 381–385 (2020).
22. C. Wang, Y. Gao, D. Xiao, *Phys. Rev. Lett.* **127**, 277201 (2021).
23. H. Liu et al., *Phys. Rev. Lett.* **127**, 277202 (2021).
24. S. Lahiri, K. Das, D. Culcer, A. Agarwal, Intrinsic nonlinear conductivity induced by the quantum metric dipole. Preprint at <https://arxiv.org/abs/2207.02178> (2022).
25. T. B. Smith, L. Pullasser, A. Srivastava, *Phys. Rev. Res.* **4**, 013127 (2022).
26. A. Arora, M. S. Rudner, J. C. W. Song, *Nano Lett.* **22**, 9351–9357 (2022).
27. J. Mitscherling, T. Holder, *Phys. Rev. B* **105**, 085154 (2022).
28. J.-W. Rhim, K. Kim, B.-J. Yang, *Nature* **584**, 59–63 (2020).
29. P. J. Ledwith, G. Tarnopolsky, E. Khalaf, A. Vishwanath, *Phys. Rev. Res.* **2**, 023237 (2020).
30. T. Holder, D. Kaplan, B. Yan, *Phys. Rev. Res.* **2**, 033100 (2020).
31. H. Watanabe, Y. Yanase, *Phys. Rev. X* **11**, 011001 (2021).
32. K.-E. Huhtinen, J. Herzog-Arbeitman, A. Chew, B. A. Bernevig, P. Törmä, *Phys. Rev. B* **106**, 014518 (2022).
33. J. S. Hofmann, E. Berg, D. Chowdhury, *Phys. Rev. Lett.* **130**, 226001 (2023).
34. X. Hu, T. Hyart, D. I. Pikulin, E. Rossi, *Phys. Rev. B* **105**, L140506 (2022).
35. N. Nagaosa, J. Sinova, S. Onoda, A. MacDonald, N. P. Ong, *Rev. Mod. Phys.* **82**, 1539–1592 (2010).
36. M. M. Otrokov et al., *Nature* **576**, 416–422 (2019).
37. D. Zhang et al., *Phys. Rev. Lett.* **122**, 206401 (2019).
38. S. H. Lee et al., *Phys. Rev. Res.* **1**, 012011 (2019).
39. Y. Deng et al., *Science* **367**, 895–900 (2020).
40. C. Liu et al., *Nat. Mater.* **19**, 522–527 (2020).
41. H. Deng et al., *Nat. Phys.* **17**, 36–42 (2021).
42. D. Ovchinnikov et al., *Nano Lett.* **21**, 2544–2550 (2021).
43. S. Yang et al., *Phys. Rev. X* **11**, 011003 (2021).
44. A. Gao et al., *Nature* **595**, 521–525 (2021).
45. L. Tai et al., *ACS Nano* **16**, 17336–17346 (2022).
46. S.-K. Bac et al., *npj Quantum Mater.* **7**, 46 (2022).
47. T. Akamatsu et al., *Science* **372**, 68–72 (2021).
48. A. Iyama, T. Kimura, *Phys. Rev. B* **87**, 180408 (2013).
49. S. Jiang, J. Shan, K. F. Mak, *Nat. Mater.* **17**, 406–410 (2018).
50. H. Zhang et al., *Nat. Phys.* **5**, 438–442 (2009).
51. J. Kipp et al., *Commun. Phys.* **4**, 99 (2021).
52. A. Gao, S. Xu, Quantum metric nonlinear Hall effect in a topological antiferromagnetic heterostructure, Zenodo (2023); <https://doi.org/10.5281/zenodo.8002209>.

ACKNOWLEDGMENTS

We are grateful to A. Yacoby for help with the microwave measurements. We thank M. Wesson and N. Poniatoski for technical support during the microwave measurements. We also thank Y. Gao, J. Ahn, and P. Kim for helpful discussions. We are grateful to L. Ye, M. Mogi, Y. Fujishiro, and T. Kurumaji for extensive discussions on the scaling of AHE. **Funding:** Work in the S.-Y.X. group was partly supported through the Center for the Advancement of Topological Semimetals (CATS), an Energy Frontier Research Center (EFRC) funded by the US Department of

Energy (DOE) Office of Science (fabrication and measurements), through the Ames National Laboratory under contract DE-AC0207CH11358, and partly through Air Force Office of Scientific Research (AFOSR) grant FA9550-23-1-0040 (data analysis and manuscript writing). S.-Y.X. acknowledges the Corning Fund for Faculty Development. Q.M. and L.F. acknowledge support from the NSF Convergence program (NSF ITE-2235945) and the CIFAR program. S.-Y.X. and D.B. were supported by the NSF Career DMR-2143177. C.T. and Z.S. acknowledge support from the Swiss National Science Foundation under project P2EZP2 191801 and P500PT 206914, respectively. Y.F.L., S.-Y.X., D.C.B., Y.O., and L.F. were supported by the STC Center for Integrated Quantum Materials (CIQM), NSF grant no. DMR-1231319. This work was performed in part at the Center for Nanoscale Systems (CNS) Harvard University, a member of the National Nanotechnology Coordinated Infrastructure Network (NNCI), which is supported by the National Science Foundation under NSF award no. 1541959. Bulk single-crystal growth and characterization of MnBi₂Te₄ were performed at UCLA and were supported by the DOE, Office of Science, under award no. DE-SC0021117. The work at Northeastern University was supported by the Air Force Office of Scientific Research under award no. FA9550-20-1-0322, and it benefited from the computational resources of Northeastern University's Advanced Scientific Computation Center (ASCC) and the Discovery Cluster. The work in the QM group was partly supported through the CATS, an EFRC funded by the DOE Office of Science, through the Ames National Laboratory under contract DE-AC0207CH11358 (fabrication and measurements) and partly through NSF DMR-2143426 (data analysis and manuscript writing). T.V.T. and P.P.O. were supported by the CATS, an EFRC funded by the DOE Office of Science, through the Ames National Laboratory under contract DE-AC0207CH11358. T.R.C. was supported by the 2030 Cross-Generation Young Scholars Program of the National Science and Technology Council (NSTC) in Taiwan (program no. MOST111-2628-M-006-003-MY3); National Cheng Kung University (NCKU), Taiwan; and the National Center for Theoretical Sciences (NCTS), Taiwan. This research was supported, in part, by the Higher Education Sprout Project, Ministry of Education to the Headquarters of University Advancement at NCKU. H.L. acknowledges support from the National Science and Technology Council (NSTC) in Taiwan under grant no. MOST 111-2112-M-001-057-MY3. The work at TIFR Mumbai was supported by the Department of Atomic Energy of the Government of India under project no. 12-R&D-TFR-5.10-0100 and benefited from the computational resources of TIFR Mumbai. K.W. and T.T. acknowledge support from the JSPS KAKENHI (grant nos. 20H00354, 21H05233, and 23H02052) and World Premier International Research Center Initiative (WPI), MEXT, Japan. M.H. and C.R.D. were supported by the AFOSR under award no. FA9550-20-1-0319. S.W.C. acknowledges partial support from the Harvard Quantum Initiative in Science and Engineering.

Author contributions: S.-Y.X. conceived the experiments and supervised the project. A.G. fabricated the devices, performed the measurements, and analyzed data with help from Y.F.L., D.B., J.X.Q., H.C.L., C.T., T.D., Z.S., S.C.H., D.C.B., and Q.M. A.G. and S.W.C. performed the microwave rectification experiments. C.H., T.Q., and N.N. grew the MnBi₂Te₄ single crystals. M.H. and C.R.D. performed NV center magnetometry. B.G. made the theoretical studies, including first-principles calculations and effective modeling, with the help from T.V.T., Y.O., H.J.T., S.W.L., B.S., H.L., A.B., T.R.C., L.F., and P.P.O. T.V.T. developed the effective model with help from B.G. under the guidance of P.P.O. K.W. and T.T. grew the hBN single crystals. S.-Y.X., A.G., and Q.M. wrote the manuscript with input from all authors. **Competing interests:** The authors declare no competing financial interests. **Data and materials availability:** Data in the main text and supplementary materials, as well as the codes for theoretical calculations of the quantum metric, are available from Zenodo (52). **License information:** Copyright © 2023 the authors, some rights reserved; exclusive licensee American Association for the Advancement of Science. No claim to original US government works. <https://www.sciencemag.org/about/science-licenses-journal-article-reuse>

SUPPLEMENTARY MATERIALS

science.org/doi/10.1126/science.adf1506
Materials and Methods
Supplementary Text
Figs. S1 to S50
Tables S1 to S3
References (53–71)

Submitted 5 October 2022; accepted 6 June 2023
Published online 15 June 2023
[10.1126/science.adf1506](https://doi.org/10.1126/science.adf1506)